STRUCTURAL BIOLOGY

ISSN 2059-7983

Molecular architecture of the nucleoprotein C-terminal domain from the Ebola and Marburg viruses

Laura E. Baker,[a,b] Jeffrey F. Ellena,[c] Katarzyna B. Handing,[a] Urszula Derewenda,[a] Darkhan Utepbergenov,[a]‡ Daniel A. Engel[b] and Zygmunt S. Derewenda[a]*

[a]Department of Molecular Physiology and Biological Physics, University of Virginia School of Medicine, Charlottesville, VA 22908-0736, USA, [b]Department of Microbiology, Immunology and Cancer Biology, University of Virginia School of Medicine, Charlottesville, VA 22908-0736, USA, and [c]Department of Chemistry, University of Virginia, Charlottesville, VA 22904-4319, USA. *Correspondence e-mail: zsd4n@virginia.edu

Received 16 July 2015
Accepted 11 November 2015

Edited by E. F. Garman, University of Oxford, England

‡ Current address: Department of Chemistry, Nazarbayev University, 53 Kabanbay Batyr Avenue, Astana 010000, Kazakhstan.

Keywords: viral proteins; *Ebolavirus*; *Marburgvirus*; nucleoprotein; *Filoviridae*.

PDB references: C-terminal domain of Ebola (Bundibugyo) nucleoprotein, 5dsd; C-terminal domain of Ebola (Taï Forest) nucleoprotein, 5e2x

Supporting information: this article has supporting information at journals.iucr.org/d

The *Filoviridae* family of negative-sense, single-stranded RNA (ssRNA) viruses is comprised of two species of *Marburgvirus* (MARV and RAVV) and five species of *Ebolavirus*, *i.e.* Zaire (EBOV), Reston (RESTV), Sudan (SUDV), Taï Forest (TAFV) and Bundibugyo (BDBV). In each of these viruses the ssRNA encodes seven distinct proteins. One of them, the nucleoprotein (NP), is the most abundant viral protein in the infected cell and within the viral nucleocapsid. It is tightly associated with the viral RNA in the nucleocapsid, and during the lifecycle of the virus is essential for transcription, RNA replication, genome packaging and nucleocapsid assembly prior to membrane encapsulation. The structure of the unique C-terminal globular domain of the NP from EBOV has recently been determined and shown to be structurally unrelated to any other known protein [Dziubańska *et al.* (2014), *Acta Cryst*. D**70**, 2420–2429]. In this paper, a study of the C-terminal domains from the NP from the remaining four species of *Ebolavirus*, as well as from the MARV strain of *Marburgvirus*, is reported. As expected, the crystal structures of the BDBV and TAFV proteins show high structural similarity to that from EBOV, while the MARV protein behaves like a molten globule with a core residual structure that is significantly different from that of the EBOV protein.

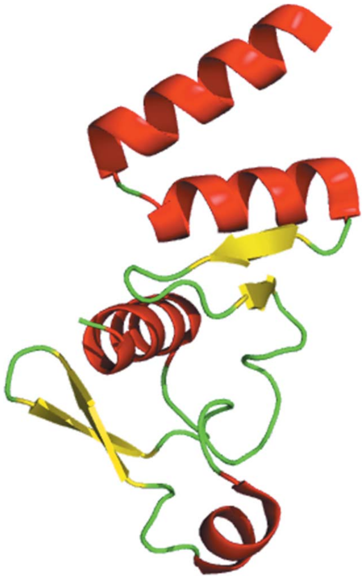

1. Introduction

Most viruses of the *Ebolavirus* and *Marburgvirus* genera, which comprise the *Filoviridae* family within the order *Mononegavirales*, cause severe hemorrhagic fever in humans. The ongoing outbreak of Ebola virus disease (EVD) in West Africa demonstrates the grave threat that filoviruses pose globally to human health. While the EVD outbreak is slowly losing momentum, it is still unprecedented, resulting in over 23 000 cases and more than 9000 deaths when this manuscript was in preparation (according to Center for Disease Control data). The epidemic spread more extensively and rapidly than in past outbreaks, beginning in Guinea in December 2013 and then spreading throughout Guinea, Liberia and Sierra Leone (Baize *et al.*, 2014). The current epidemic is caused by a variant of the Zaire strain (EBOV), one of five currently known *Ebolavirus* species. The other four are Taï Forest (TAFV), Bundibugyo (BDBV), Reston (RESTV) and Sudan (SUDV) (Bukreyev *et al.*, 2014). EBOV, SUDV and BDBV have all

http://dx.doi.org/10.1107/S2059798315021439

caused large outbreaks of EVD in the past (Roddy *et al.*, 2012; Feldmann & Geisbert, 2011), while TAFV has so far been reported in only one patient (Formenty *et al.*, 1999). The five *Ebolavirus* species vary with respect to their corresponding fatality rates: RESTV is nonpathogenic to humans and SUDV and BDBV have fatality rates of about 40%, while EBOV has had a fatality rate of up to 90% in the past, although in the current outbreak it has been significantly lower. The fatality rate in the only two significant outbreaks of Marburg fever, caused by MARV infection, was also ~90% (Brauburger *et al.*, 2012). The molecular basis underlying this variation in fatality rate is not known.

Like other viruses in the *Mononegavirales* order, *Ebolavirus* and the closely related *Marburgvirus* are membrane-enveloped viruses which contain negative-sense, single-stranded RNA (ssRNA) encoding seven genes that owing to co-transcriptional and post-translational processes generate more than seven proteins. Two of them are associated with the membrane: the glycoprotein (GP), which is a transmembrane protein, and VP40, which is associated with the inner surface of the membrane. The remaining five principal proteins [*i.e.* the nucleoprotein (NP), VP35, VP30, VP24 and RNA polymerase (L)] all interact with ssRNA to form the nucleocapsid (Beniac *et al.*, 2012; Bharat *et al.*, 2012; Mühlberger *et al.*, 1999). The critical protein responsible for the assembly of the nucleocapsid is the NP. It is a 739-residue (EBOV) single polypeptide chain, with an N-terminal region (approximately 1–400) that is engaged in packaging the ssRNA (Watanabe *et al.*, 2006) and a C-terminal region that is largely unstructured and which is implicated in several protein–protein interactions (Noda *et al.*, 2007; Shi *et al.*, 2008; Licata *et al.*, 2004). We have recently shown that this region contains a unique globular domain (NP^{Ct}; residues 641–739) and we have determined its crystal structure (Dziubańska *et al.*, 2014). Crystallographic studies have also been reported for the N-terminal globular domain with and without a peptide derived from VP35 (PDB entries 4ypi, 4z9p and 4ztg; Leung *et al.*, 2015; Dong *et al.*, 2015; Kirchdoerfer *et al.*, 2015).

Interestingly, the NP^{Ct} contains one of the most divergent amino-acid sequences among the proteins encoded by the *Filoviridae*. Pairwise sequence comparisons between the five *Ebolavirus* species show amino-acid identity ranging from 60 to 85%, while the NP^{Ct} from MARV contains only 12 residues found in the *Ebolavirus* consensus sequence. In this context, it is interesting to note that the nucleocapsids of *Ebolavirus* and *Marburgvirus* exhibit differences in their structures, suggesting functional variation among the respective nucleoproteins (Watanabe *et al.*, 2006; Kolesnikova *et al.*, 2000; Mavrakis *et al.*, 2002; Huang *et al.*, 2002; Noda *et al.*, 2006). In an effort to gain more understanding of the sequence–function relationships in the nucleoproteins from *Filoviridae*, we have undertaken a study of the NP^{Ct} domains from other species of *Ebolavirus* and from MARV. In this paper, we report the crystal structures of the NP^{Ct} from BDBV and TAFV, and the surprising results of NMR studies of the MARV NP^{Ct}, attesting to critical differences between the *Ebolavirus* and *Marburgvirus* nucleoproteins.

2. Materials and methods

2.1. Preparation of recombinant proteins

2.1.1. Cloning, expression and purification. cDNA constructs coding for the 641–739 fragments of TAFV, BDBV and RESTV NP, as well as the 641–738 fragment of SUDV NP and the 600–695 fragment of MARV NP, were synthesized commercially (GENEWIZ) using optimized codon frequencies for *Escherichia coli*. The constructs were cloned into the MBP-His$_6$-Parallel1 vector with an rTEV cleavage site downstream of His$_6$ (Sheffield *et al.*, 1999).

Briefly, BL21-CodonPlus (DE3)-RIPL *E. coli* cells (Stratagene) were grown in Terrific Broth at 37°C. Induction was carried out at an OD$_{600}$ of ~2.5 with the addition of 0.5 m*M* IPTG after the temperature of the culture was decreased to 16°C, and growth continued for 18 h. The cells were harvested by centrifugation and the pellet was frozen at −20°C. The pellet was resuspended in 5 ml lysis buffer (50 m*M* Tris–HCl, 300 m*M* NaCl, 5 m*M* β-mercaptoethanol pH 7.5) per gram of pellet. Cells were disrupted with a Dounce homogenizer and sonication (Branson Sonifier 450) and were centrifuged at 35 000 rev min^{-1} (45 Ti rotor) for 45 min. The supernatant was applied onto an Ni–NTA gravitational column (5 ml resin; Qiagen). The column was washed with 400 ml lysis buffer and the recombinant protein was eluted with 50 m*M* Tris–HCl, 300 m*M* NaCl, 5 m*M* β-mercaptoethanol, 250 m*M* imidazole pH 7.5. The affinity tags were removed by incubating the recombinant protein with rTEV protease with concomitant dialysis against 4 l dialysis buffer (50 m*M* Tris–HCl, 300 m*M* NaCl, 5 m*M* β-mercaptoethanol pH 7.5) overnight. The protein solution was then applied onto an Ni–NTA column and the flowthrough containing NP^{Ct} was collected, followed by a 30 ml wash with the same buffer. Samples concentrated using Amicon microconcentrators with a 3000 Da cutoff were subjected to size-exclusion chromatography on a Superdex 75 column connected to a GE Healthcare ÄKTA system and equilibrated with 50 m*M* Tris–HCl, 150 m*M* NaCl, 5 m*M* β-mercaptoethanol pH 7.5 at 4°C. Fractions containing NP^{Ct} were pooled. The BDBV NP^{Ct} fusion protein (MBP-His$_6$-BDBV) was also purified using an amylose resin column (Qiagen) according to the manufacturer's instructions to achieve higher purity prior to cleavage.

2.1.2. Preparation of ^{15}N-labeled and ^{13}C,^{15}N-labeled MARV NP^{Ct}. ^{15}N-Labeled and ^{13}C,^{15}N-labeled MARV NP^{Ct} samples were expressed as described previously for the EBOV NP^{Ct} (Dziubańska *et al.*, 2014). Labeled proteins were purified in exactly the same manner as unlabeled MARV NP^{Ct}, except that the buffer for size-exclusion chromatography consisted of 40 m*M* HEPES, 150 m*M* NaCl, 5 m*M* β-mercaptoethanol pH 7.5. For assignment experiments, a sample of 500 µ*M* ^{15}N-NP^{Ct} and 950 µ*M* ^{13}C,^{15}N-NP^{Ct} in 40 m*M* HEPES, 150 m*M* NaCl, 5 m*M* β-mercaptoethanol pH 7.5 buffer supplemented with 5% D_2O was prepared.

2.2. Thermal stability assays

The midpoint melting temperature (T_m) of protein samples was determined by monitoring the fluorescence of SYPRO

Table 1
Crystallization data and refinement statistics for the NP^{Ct} domain from TAFV and BDBV.

Values in parentheses are for the highest resolution shell.

	TAFV NP^{Ct}	BDBV NP^{Ct}
Data collection		
Wavelength (Å)	0.9792	0.9900
Space group	$P1$	$P6_422$
Z	8	12
Unit-cell parameters (Å, °)	a = 57.85, b = 60.08, c = 73.55, α = 69.15, β = 68.94, γ = 89.9	a = b = 60.08, c = 82.74
Resolution (Å)	50.00–2.10 (2.14–2.10)	80.00–2.30 (2.38–2.30)
Completeness (%)	96.1 (84.6)	94.3 (64.7)
Total observations	103077	184210
Mean $I/\sigma(I)$	12.4 (1.9)	31.3 (1.9)
$CC_{1/2}$	(0.789)	(0.981)
Multiplicity	2.1 (2.0)	14.8 (7.1)
$R_{\rm merge}$† (%)	0.070 (0.316)	0.084 (0.432)
Structure refinement		
Unique reflections	48012	12396
Reflections in $R_{\rm free}$ set	2235	604
R‡ (%)	19.1	16.1
$R_{\rm free}$‡ (%)	26.0	20.2
R.m.s.d., bond lengths (Å)	0.007	0.008
R.m.s.d., bond angles (°)	1.1	1.3
No. of atoms		
Protein atoms	6738	870
O atoms from waters	664	113
Ligand/ion atoms	73	13
Mean B value (Å^2)		
Overall	42	82
Protein atoms (Å^2)	42	82
O atoms from waters (Å^2)	45	79
Ligand/ion atoms (Å^2)	47	116
Clashscore	0.08	0.00
Clashscore percentile (%)	100	100
Rotamer outliers (%)	1.76	1.09
Ramachandran outliers (%)	0.00	0.00
Ramachandran favored (%)	99.61	99.01

† $R_{\rm merge} = \sum_{hkl}\sum_i |I_i(hkl) - \langle I(hkl)\rangle| / \sum_{hkl}\sum_i I_i(hkl)$, where $\langle I(hkl)\rangle$ is the mean of i observations $I_i(hkl)$ of reflection hkl. ‡ R factor and $R_{\rm free} = \sum_{hkl} \big||F_{\rm obs}| - |F_{\rm calc}|\big| / \sum_{hkl} |F_{\rm obs}|$, where $F_{\rm obs}$ and $F_{\rm calc}$ are the observed and calculated structure factors, respectively, calculated for recorded data (R factor) and for 5% of the data which were omitted in refinement ($R_{\rm free}$).

Orange dye (Life Technologies) in the presence of the protein as a function of temperature (Ericsson *et al.*, 2006). Assays were performed in 20 µl containing 20 µg protein, with the concentration of the dye as recommended by the manufacturer (*i.e.* 1000× dilution of the DMSO stock, followed by 5× dilution in the final sample) and buffer (50 m*M* Tris–HCl, 150 m*M* NaCl, 5 m*M* β-mercaptoethanol pH 7.5). Fluorescence was recorded as a function of temperature from 20 to 90°C using an Applied Biosystems StepOnePlus Real-Time PCR System (Life Technologies). This instrument uses wavelengths of 488 nm for excitation and 586 nm for emission. The *StepOne* software (v.2.1) was used for data processing and figure preparation.

2.3. Crystallization of NP^{Ct}

All crystallization experiments were carried out using the sitting-drop vapor-diffusion method in crystallization screens set up with a Mosquito robot (TTP Labtech). Protein samples were concentrated to ∼10–20 mg ml^{-1}. Three commercial screens were used, JCSG+, PEG/Ion and SaltRX, in a canonical setting or using the alternative reservoir approach (Newman, 2005). For each crystallization condition, 1:1 and 2:1 ratios of precipitant to protein solution were used, with a drop volume of 200–250 nl.

2.4. Data collection and structure determination

Crystals were cryoprotected under a range of conditions and then screened for diffraction quality. The crystals of TAFV NP^{Ct} used for final data collection were flash-cooled directly from the crystallization drop. Those of BDBV NP^{Ct} that subsequently gave the best diffraction were soaked in 1.5 *M* $LiSO_4$, 0.075 *M* Tris pH 8.5, 20% glycerol. All crystals were flash-cooled by immersion into liquid nitrogen. X-ray data were collected at ∼100 K on the SER-CAT beamlines (Southeast Regional Collaborative Access Team) at the Advanced Photon Source, Argonne National Laboratory. Data were indexed, integrated and scaled with *HKL*-3000

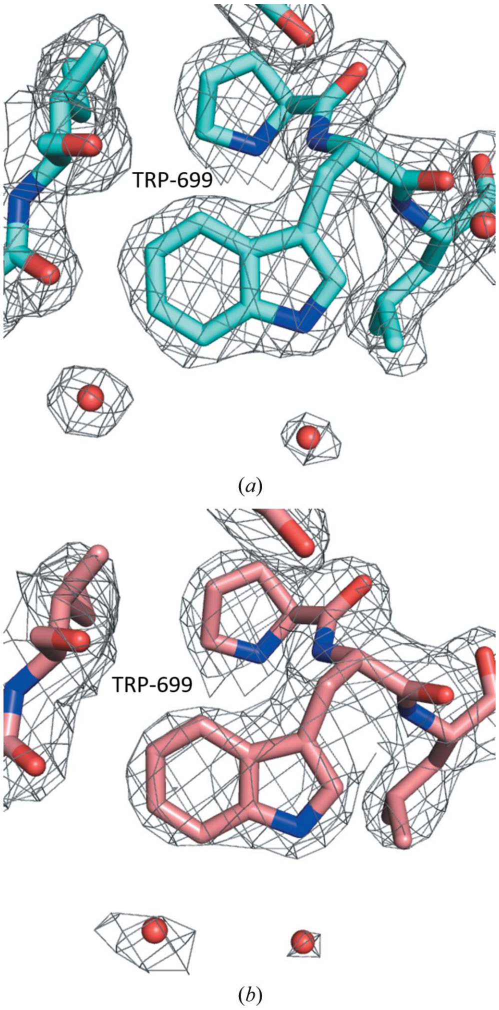

Figure 1
Representative electron-density map ($2F_{\rm o} - F_{\rm c}$) centered on Trp669 for TAFV NP^{Ct}. (*a*) Analogous electron density for the same structural element in BDBV NP^{Ct}. (*b*) The electron-density map is contoured at the 1σ level; O atoms are shown in red, N atoms in blue and C atoms in magenta and pink (for TAFV and BDBV, respectively).

Table 2
Thermal stability of NP^{Ct} domains from various Ebola strains.

Species of *Ebolavirus*	Midpoint of unfolding (°C)
ZEBOV	56.9
TAFV	52.8
BDBV	50.8
SUDV	48.5
RESTV	48.3

(Minor *et al.*, 2006). Table 1 gives details of the data-processing statistics.

The structure of TAFV NP^{Ct} was solved at 2.1 Å resolution by molecular replacement (MR) using *MOLREP* (Vagin & Teplyakov, 2010) operated within the *HKL*-3000 interface (Minor *et al.*, 2006). The crystal structure of the NP^{Ct} from EBOV (PDB entry 4qb0; Dziubańska *et al.*, 2014) was used as a search model to obtain the initial phases. The structure of the BDBV NP^{Ct} was determined at 2.3 Å resolution using the same search model and *Phaser* (Bunkóczi *et al.*, 2013) as implemented in *PHENIX* (Adams *et al.*, 2010). Refinement of both structures was performed with *REFMAC*5 (Murshudov *et al.*, 2011) within *HKL*-3000, with *Coot* (Emsley *et al.*, 2010), allowing manual intervention, and with the *CCP*4 suite (Winn *et al.*, 2011). TLS (translation/libration/screw) refinement was used in the next stage of refinement, and TLS groups were determined using the *TLSMD* server (Painter & Merritt, 2006). Individual isotropic displacement parameters were used from this point onwards. Water molecules were added in several stages during the refinement automatically and were reviewed visually. The standalone version of the *MolProbity* server (Chen *et al.*, 2010) and the *PDB Validation Server* were both used for structure validation (Berman *et al.*, 2000). Crystal contacts were analyzed using the *PISA* server (Krissinel & Henrick, 2007). The final electron-density maps are of high quality and are easily interpretable (Fig. 1). Refinement statistics are summarized in Table 1.

2.5. Heteronuclear NMR

A Bruker Avance III 600 MHz spectrometer equipped with a cryoprobe was used to obtain NMR spectra at 25°C. *NMRPipe* (Delaglio *et al.*, 1995) was used to process the spectral data. *CcpNmr Analysis* v.2 (Vranken *et al.*, 2005) and *Sparky* 3 (T. D. Goddard & D. G. Kneller, University of California, San Francisco, USA) were used for spectrum visualization and sequential assignment of backbone and C^{β}, ^{1}H (except H^{α}), ^{13}C and ^{15}N resonances. *TALOS-N* was used for used for estimation of secondary structure (Shen & Bax, 2013).

2.6. Sequence and structure analysis

PyMOL (Schrödinger) was used to align structures and to calculate r.m.s.d. values between superposed structures with cycles and transform parameters set to zero. *PyMOL* was also used to generate figures. The *STRIDE* server (Heinig & Frishman, 2004) was used for assignment of two-dimensional structure elements from atomic resolution structures.

3. Results and discussion

3.1. Expression and purification

All five C-terminal domains of NP under study, *i.e.* from TAFV, BDBV, SUDV, RESTV and MARV, were overexpressed in *E. coli* as fusion proteins with an N-terminal MBP-His_6 double tag, cleaved from the tag with rTEV and purified to homogeneity as described above (Supplementary Fig. S1). The final yields were approximately 10–15 mg pure protein per litre of culture.

3.2. Thermal stability

To ascertain that the expressed proteins are folded into stable modules in solution, we tested all five using a thermal shift assay which utilizes the dye SYPRO Orange. Table 2 lists the values for the temperature midpoints of cooperative unfolding determined for the five strains of EBOV. All fall within a relatively narrow range between 48.3 and 52.8°C, consistent with previous results obtained for the EBOV protein (Dziubańska *et al.*, 2014). Unexpectedly, no thermal unfolding was observed for the MARV NP^{Ct} (Supplementary Fig. S2).

3.3. Crystallization

Crystallization screens were set up as described above. Of the five proteins screened, the NP^{Ct} domains from TAFV and BDBV both yielded X-ray-quality single crystals, while those from RESTV, SUDV and MARV did not.

For the TAFV NP^{Ct}, initial crystals appeared in the JCSG+ screen in a range of solution including those consisting of (i) 20% PEG 8000, 0.1 *M* CHES pH 9.5; (ii) 10% PEG 6000, 0.1 *M* HEPES pH 7; and (iii) 20% PEG 8000, 0.2 *M* $MgCl_2$, 0.1 *M* HEPES pH 7. Based on these observations, crystallization was optimized using a 1:1 ratio of precipitant (10% PEG 3350, 0.027 *M* HEPES/0.073 *M* Tris pH 8.6) to protein solution, with a protein concentration of ~5.0 mg ml^{-1} and a 1.5 *M* NaCl reservoir. The crystals belonged to space group *P*1 and diffracted to 2.1 Å.

In the case of the BDBV NP^{Ct}, initial crystals appeared in a 1:1 mixture with 1.5 *M* lithium sulfate monohydrate, 0.1 *M* Tris pH 8.5 (SaltRx) equilibrated against a reservoir containing the screen solution. These conditions were used as a starting point for optimization, which led to single crystals suitable for X-ray experiments, which were grown using a 1:1 ratio of reservoir (1.33 *M* $LiSO_4$, 0.1 *M* Tris pH 8.5) to protein solution with a protein concentration of 13.9 mg ml^{-1}. The crystals exhibited the symmetry of space group $P6_222$ or $P6_422$ and diffracted to 2.3 Å resolution.

The SUDV protein crystallized in a number of conditions containing PEG 3350, but the crystals did not diffract well in spite of extensive efforts to improve them. Neither the RESTV nor the MARV proteins formed crystals in any of the screens. Efforts to crystallize MARV were discontinued in favor of an heteronuclear NMR study, which is described below.

Table 3
Comparison of structural changes in the characterized *Ebolavirus* NP^{Ct} structures expressed by C^{α} r.m.s.d. value.

Left, C^{α} r.m.s.d. of the NP^{Ct} structure (fragment 645–739); right, C^{α} r.m.s.d. of the core of the NP^{Ct} domain (αB, β1, β2 and αD).

C^{α} all/C^{α} core (Å)	EBOV (PDB entry 4qb0)	EBOV (PDB entry 4qaz)	TAFV chain *A*	TAFV chain *E*
EBOV (PDB entry 4qaz)	1.2/0.6			
TAFV chain *A*	1.9/0.7	1.9/0.7		
TAFV chain *E*	1.3/0.6	1.4/0.6	1.2 0.3	
BDBV	1.3/0.9	1.5/0.6	1.8/0.5	1.3/0.4

3.4. The crystal structures of the Taï Forest and Bundibugyo NP^{Ct} domains

3.4.1. Overview. In general terms, the two crystal structures determined in our study show high similarity to the NP^{Ct} domain from EBOV, the structure of which has been reported by us previously (Dziubańska *et al.*, 2014). This was of course expected given the 82% sequence identity between the BDBV and EBOV proteins, the 79% sequence identity between the TAFV and EBOV proteins, and the 86% sequence identity between the BDBV and TAFV proteins. The tertiary fold is the same: there are two α-helices at the N-terminus (αA and αB) folded into an antiparallel hairpin, followed by two antiparallel β-strands (β1 and β2), a coil fragment containing another short α-helix (αC) and another pair of antiparallel β-strands (β3 and β4); finally, the C-terminal α-helix (αD) which inserts itself between the two β-hairpins provides a number of hydrophobic interactions at the core (Fig. 2). The superposition of the C^{α} models presented here on EBOV NP^{Ct} (PDB entry 4qb0) shows that the core fragments, composed of αB, β1, β2 and αD, are virtually identical, as illustrated by low pairwise r.m.s.d. values of 0.3–0.9 Å (C^{α} only; see Fig. 2 and Table 3). Nevertheless, the domain shows some intrinsic flexibility, particularly with respect to the two C-terminal β-strands (β3 and β4) and the N-terminal α-helix. A comparison of crystal structures and molecular packing suggests that the slight conformational differences are more likely to be caused by packing forces and distortions owing to crystal contacts rather than genuine variation between strains. In each of the two crystal structures described here there are interesting aspects of molecular packing, and we describe those briefly below.

3.4.2. The Bundibugyo NP^{Ct} structure. The molecular-replacement calculation identified $P6_422$ as the correct space group. The atomic model of the BDBV NP^{Ct} includes the entire polypeptide comprising residues 641–739, as well as three additional residues remaining after removal of the MBP-His_6 tag from the N-terminus (Ala-Met-Ala). There is only one molecule in the asymmetric unit, with an exceptionally high solvent content of 79%, which rationalizes the high mean isothermal displacement (*B*-factor) parameter for protein atoms of 72 $Å^2$. In spite of this, the structure is relatively well resolved, with only six side chains (Lys684, Glu702, Lys703, Met706, Asp716 and Arg739) showing a significant degree of disorder.

The BDBV NP^{Ct} structure is a good example of 'minimal packing', as it shows only three intermolecular contacts, which is the smallest number required for three-dimensional packing, except for the $P2_12_12_1$ space group where only two

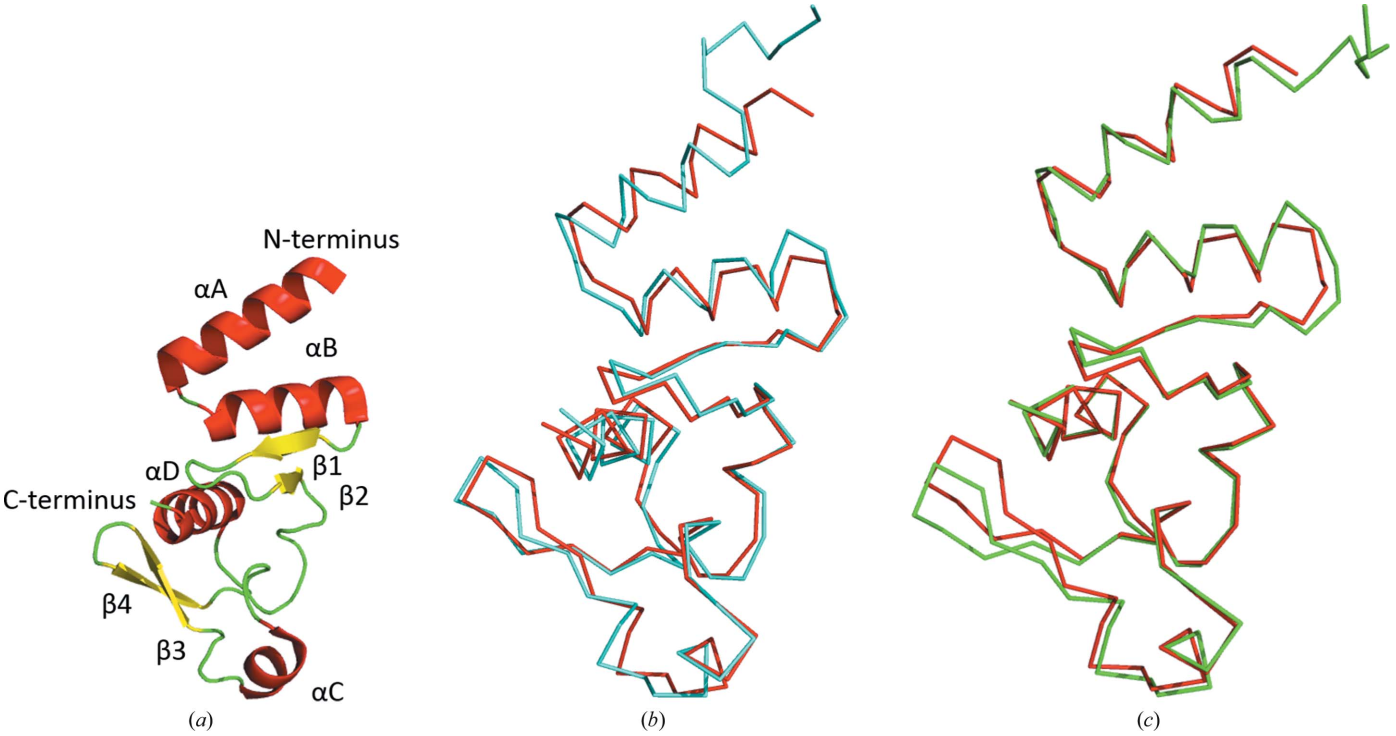

Figure 2
(*a*) The EBOV NP^{Ct} structure in cartoon representation; α-helices are shown as red ribbons and β-sheets as yellow arrows. (*b*, *c*) Superposition of EBOV NP^{Ct} (red) on TAFV NP^{Ct} (cyan) and BDBV NP^{Ct} (green), respectively. Protein models are shown in C^{α}-trace representation.

are sufficient (Wukovitz & Yeates, 1995). The first contact involves the N-terminal fragment, which includes the tripeptide from the expression vector followed by the N-terminal five amino acids that in the Zaire isoform are unstructured in the crystal. This fragment folds into an extended conformation and aligns itself next to the β1 strand of the adjacent monomer in an antiparallel fashion. This homotypic interaction creates a crystallographic dimer with a total interface of over ~1600 Å^2. The surface buried by this contact contains significant large hydrophobic patches, and the critical residues are Met639, Ala640, Gln643, Tyr668, Glu674 and Ile677 (Supplementary Fig. S3). The propensity of unstructured N-terminal fragments to mediate crystal contacts has been noted by us before and runs contrary to the assumption that one should always remove even short tags to facilitate crystallization. The second contact is mediated by the N-terminal α-helical hairpin, and also creates a crystallographic dimer, burying over 1000 Å^2 of surface in both molecules. Most of this surface is hydrophobic and is contributed by Met651, Gln659, Tyr667, Met670 and Met671. Together, these two primary contacts generate a linear ensemble of molecules lying along a threefold screw axis. The three-dimensional packing is made possible by the third contact, also homotypic, related by a twofold axis and burying over 800 Å^2. It is formed by a back-to-back packing by the C-terminal β-hairpin, with the most surface contributed by Asp709, Phe712, Gln718, Gln719 and Tyr721. As a result, six strands of molecules related by contacts 1 and 2, all lying along the threefold screws, are related by the sixfold screw axis, along which runs an enormous solvent channel providing the 79% solvent content (Fig. 3).

Given that the NP^{Ct} appears to be predominantly monomeric in solution, it is unlikely that the crystal packing has direct functional implications. However, the surfaces involved in crystal contacts, especially the distinctly hydrophobic surface of the N-terminal α-helical hairpin, may be involved in protein–protein interactions within the EBOV nucleocapsid, with the NP^{Nt} domain or perhaps between the NP and the VP40 matrix protein, the existence of which has been suggested by other studies (Licata *et al.*, 2004; Noda *et al.*, 2007; Liu *et al.*, 2011; Bharat *et al.*, 2012).

3.4.3. The Taï Forest NP^{Ct} structure. The TAFV NP^{Ct} crystal structure contains eight molecules in the asymmetric unit, although like other NP^{Ct} domains the protein is monomeric in solution as judged by gel filtration (data not shown). There is dynamic disorder that affects a number of surface residues (*i.e.* Lys641, His643–Ser647, Glu649, Glu650, Arg653, Glu657, Lys684, Glu695, Asp716, Asp717, Gln718, Gln736 and Lys739), so that there is at best a very low level of corresponding interpretable electron density for them either in one or more of the molecules. The mean isothermal displacement (*B*-factor) parameter for protein atoms in this structure is 42 Å^2. It was not possible to build the N-terminal in chains *E* and *F*, where dynamic disorder makes it difficult to model a single conformation.

The asymmetric unit may be defined as two sets of four molecules, with each set affected by different packing forces: *i.e.* chains *A*, *B*, *G* and *H* and chains *C*, *D*, *E* and *F* (Fig. 4). Within each group, the molecules adopt nearly identical conformations. However, a comparison of the C$^{\alpha}$ coordinates between the two sets (*e.g.* between the *A* and *E* chains) shows an r.m.s.d. of 1.2 Å. This difference is primarily owing to the fact that the fragment including the β3–loop–β4 in one group

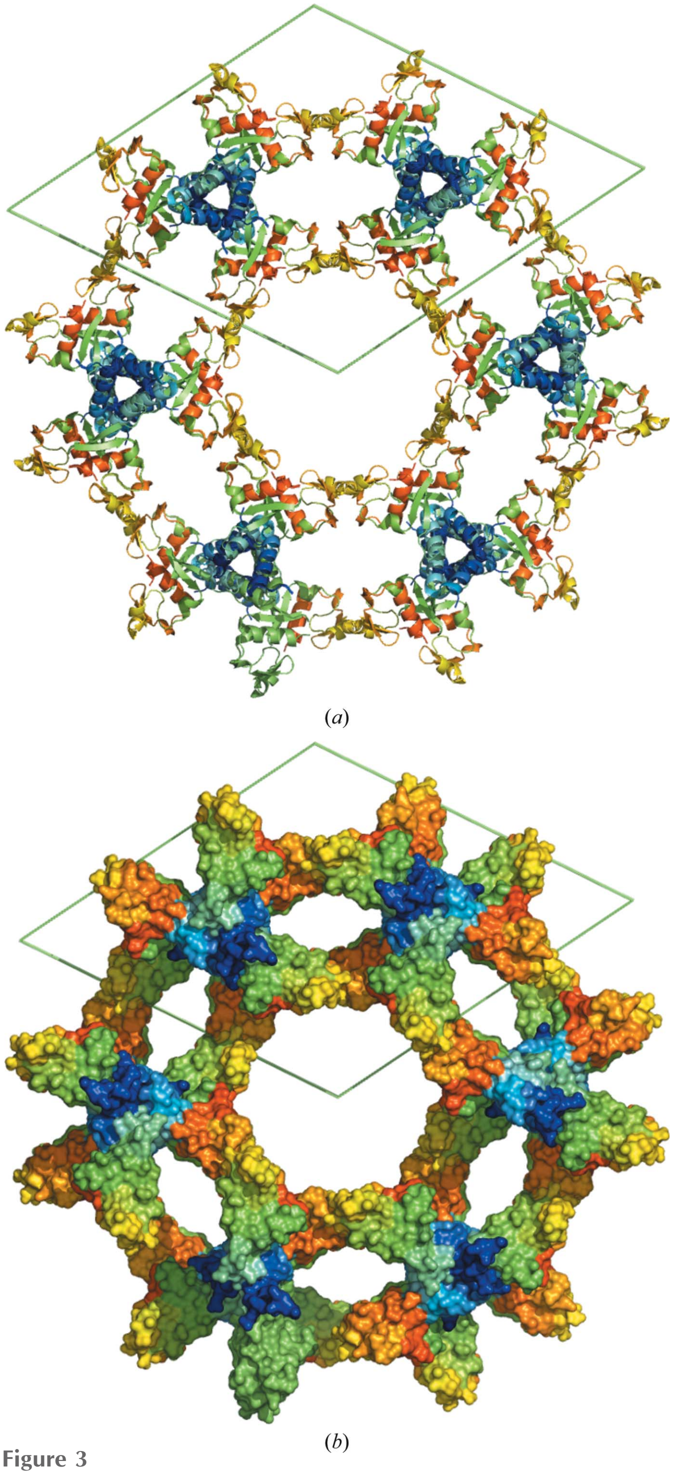

Figure 3
Molecular packing in the crystals of the BDBV NP^{Ct} domain looking down the sixfold screw axis. (*a*) Cartoon representation; coloring follows the RAINBOW option in *PyMOL*, starting with blue at the N-terminus. (*b*) Surface representation, visualizing the solvent channels; colored as in (*a*).

of molecules rotates 15.9° when compared with the other group. When only the core structure is taken into account (Table 3) the r.m.s.d. between the two is 0.3 Å.

The eight molecules in the asymmetric unit are arranged into four nearly identical noncrystallographic dimers, *i.e.* *A*/*B*, *C*/*D*, *E*/*F* and *G*/*H*. The *A*/*B* and *E*/*F* pairs are related by a noncrystallographic translation along a vector perpendicular to the *a***b* plane; the same relationship occurs between the *C*/*D* and *G*/*H* pairs. Within each dimer, the monomers are related by a twofold axis parallel to the noncrystallographic translation vector (Fig. 4). The *A*/*B*/*C*/*D* and *E*/*F*/*G*/*H* sets of molecules, along with their symmetry-related partners, each form distinct layers within the crystal. The layers are stabilized by the antiparallel hydrogen-bonded interaction of the N-termini of the *A* and *B* molecules with the β2 strands of the symmetry-related *B* and *A* chains, respectively, and *vice versa*; a symmetric set of interactions occurs between the N-termini of the *C* and *D* molecules and the β2 strands of the symmetry-related *D* and *C* molecules. Analogous crystal contacts are observed in the layer formed by the *E*/*F* and *G*/*H* dimers. The only close crystal contact between the two layers of molecules, leading to three-dimensional ordering, is between the *B* and *H* molecules.

Such high-order NCS is intriguing, given no obvious reasons that differentiate the monomers. Somewhat unexpectedly, the answer appears to lie in part in the crystallization milieu, and specifically in the presence of PEG 3350, which is used as a precipitant. Fragments of four PEG molecules were identified in this crystal structure with interpretable electron density (Fig. 5). These four fragments associate with the polypeptide chains that form the *A*/*B* and *G*/*H* dimers. All four are located in the same position on the surface of the protein between helices αA and αB, and seem to cover a distinct hydrophobic patch created by the solvent-exposed side chains of Phe662, Leu666 and Tyr669. They are also wedged into crystal contacts: in the case of the *A*/*B* dimer the PEGs mediate crystal contacts with adjacent protein molecules *C* and *D*, respectively; for the *G*/*H* dimer the contacts involve the *E* and

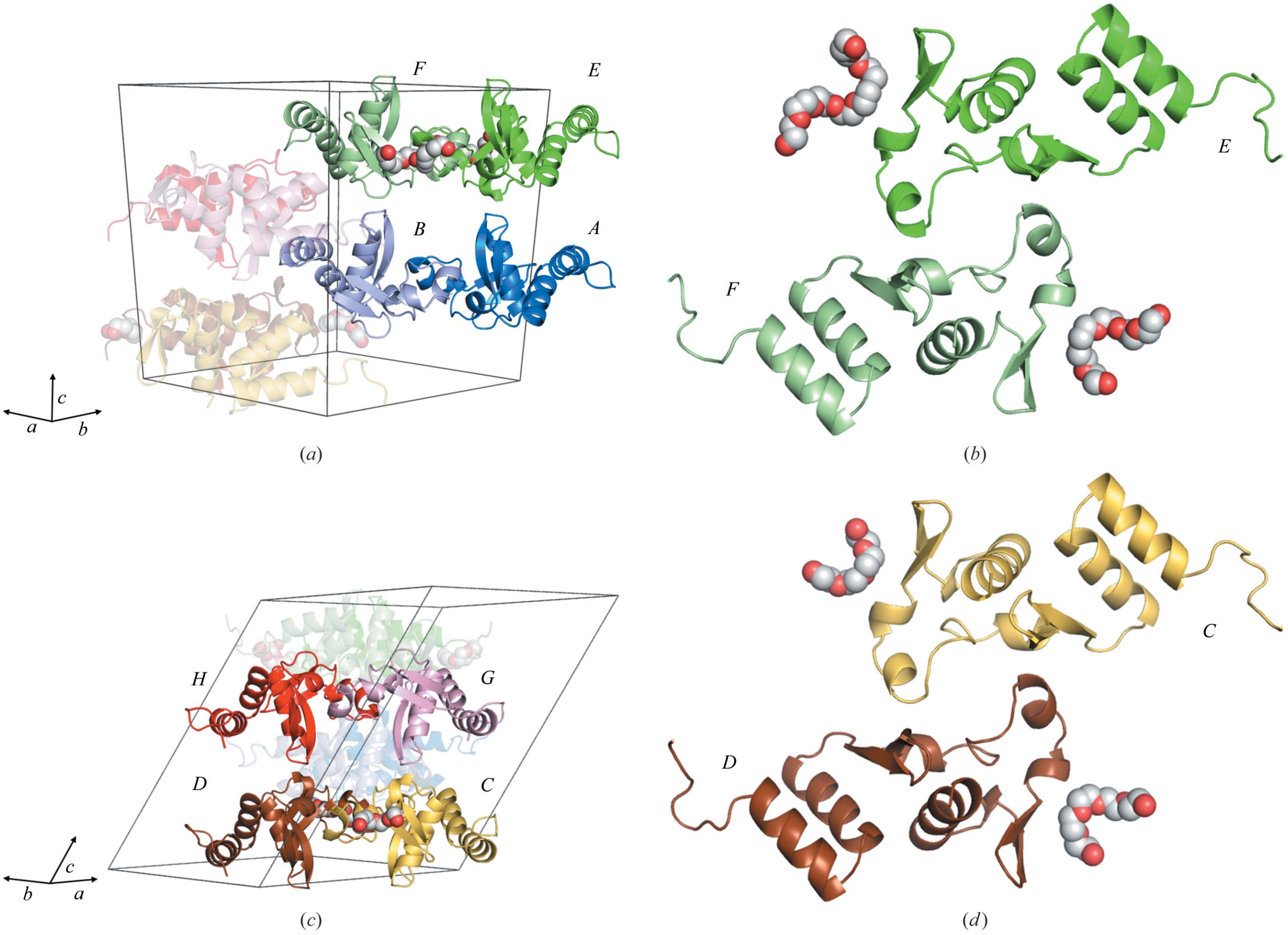

Figure 4
Molecular packing and crystal contacts in the TAFV NP$^{\rm Ct}$ crystals. (*a*) A view visualizing the *A*/*B* and *E*/*F* crystallographic dimers related by a noncrystallographic translation vector. (*b*) A view of the *A*/*B* dimer together with bound fragments of PEG 3350 down the noncrystallographic twofold axis. (*c*) A view similar to that in (*a*) of the *C*/*D* and *G*/*H* dimers. (*d*) A view of the *E*/*F* dimer together with bound fragments of PEG 3350 down the noncrystallographic twofold axis

F molecules. The binding of the PEG molecules is also correlated with the enhanced order of the N-termini: the *A*/*B* and *G*/*H* dimers have ordered N-termini, while the *C*/*D* and *E*/*F* dimers have much weaker density.

3.5. The MARV NP$^{\rm Ct}$

The lack of a detectable melting transition for this protein, along with the failure of all attempts to obtain crystals, prompted us to investigate the structure of MARV NP$^{\rm Ct}$ in solution using heteronuclear NMR. Although we expected the protein to be unfolded, the ^{15}N–^{1}H chemical shift correlation (HSQC) spectrum showed significant peak dispersion (Fig. 6). We were also able to obtain three-dimensional HNCO, HN(CA)CO, CBCA(CO)NH and HNCACB spectra and to determine the backbone (except H$^{\alpha}$) and C$^{\beta}$ assignments for 82 out of 100 residues. Nine of the unassigned residues were within a 12-residue fragment at the N-terminus. Backbone N chemical shifts were not determined for prolines. The assigned chemical shifts were used in *TALOS-N* to define secondary-structure elements. Surprisingly, the results deviated significantly from the secondary structure established for the EBOV NP$^{\rm Ct}$. The N-terminal stretch that corresponds to the α-helical hairpin in EBOV is clearly unstructured, and the second β-hairpin is replaced by a short α-helix, which evidently disrupts the tertiary structure (Fig. 7). Additional information on backbone order and dynamics was obtained by measuring N^{15} spin–lattice (R_1) and spin–spin (R_2) relaxation rates and H^1–N^{15} nuclear Overhauser effects (NOE) (Fig. 8). The spin-relaxation and NOE results indicate that the C-terminal 62 residues are relatively well ordered and the N-terminal 38 residues have low order on the nanosecond to picosecond time scale. The average H^1–N^{15} NOE for residues 634–693 was 0.75 ± 0.04. We used the average R_1R_2 value for residues 634–693 (17.6 ± 1.7 s^{-2}) to estimate an average backbone HN order parameter S^2 of 0.94 (Kneller *et al.*, 2002). Nanosecond to picosecond order can also be estimated based on chemical shifts (Berjanskii & Wishart, 2005), and these estimates (Supplementary Fig. S4) are in semi-quantitative agreement with those based on the spin-relaxation and NOE data.

We conclude that the MARV NP$^{\rm Ct}$ domain is appreciably different from the same domain in other *Ebolavirus* species, and in isolation appears to exist as a molten globule. Such moieties are known to be relatively stable and yield reasonably dispersed NMR spectra (Redfield, 2004; Walczak *et al.*,

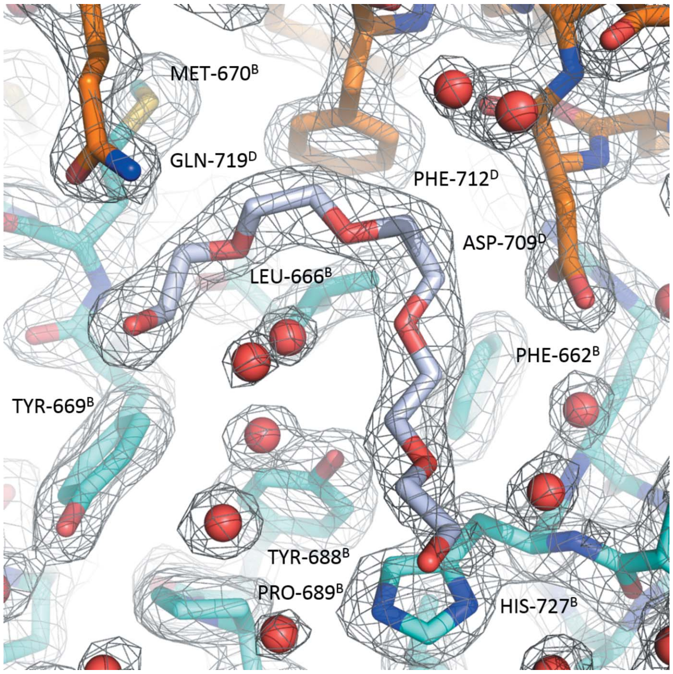

Figure 5
Representative $2F_{\rm o} - F_{\rm c}$ electron-density map contoured at the 1σ level for the PEG 3350 molecule; the PEG molecule is colored magenta and is associated with protein monomers *B* (cyan) and *D* (gold). All residues are labeled with both the number and the chain identifier. Waters are shown as red spheres.

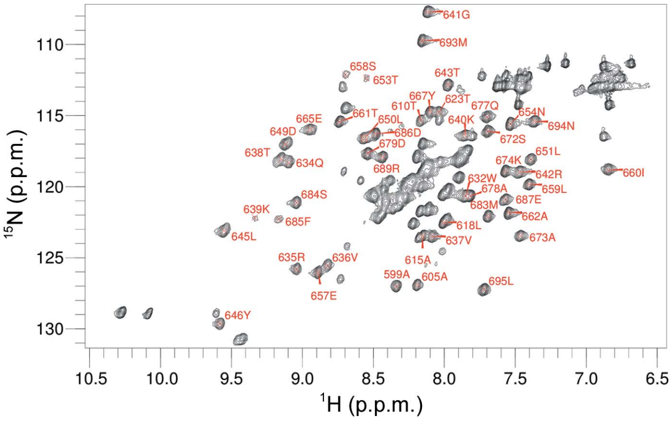

Figure 6
^{1}H–^{15}N HSQC spectrum of NP$^{\rm Ct}$ with backbone amide assignments. The two peaks with the highest ^{15}N shift are Trp indole NH. Unassigned peaks in the low-field ^{1}H–^{15}N region are owing to side chains.

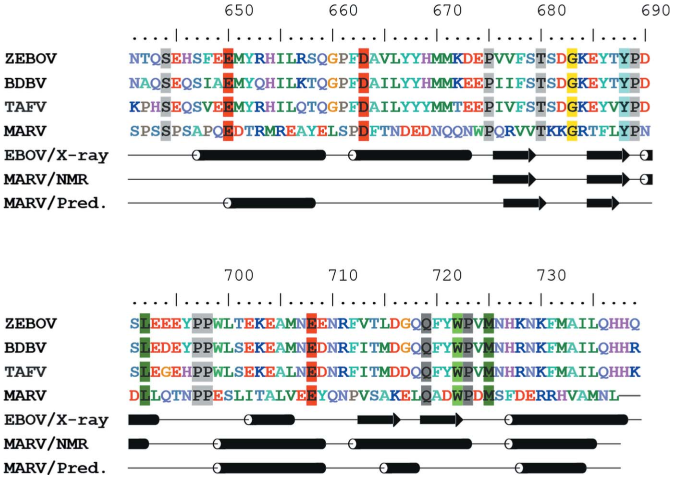
650
660
670
680
690
ZEBOV NTQSEHSFEEMYRHILRSQGPFDAVLYYHMMKDEPVVFSTSDGKEYTYPD
BDBV NAQSEQSIAEMYQHILKTQGPFDAILYYHMMKEEPIIFSTSDGKEYTYPD
TAFV KPHSEQSVEEMYRHILQTQGPFDAILYYYMMTEEPIVFSTSDGKEYVYPD
MARV SPSSPSAPQEDTRMREAYELSPDFTNDEDNQQNWPQRVVTKKGRTFLYPN
EBOV/X-ray
MARV/NMR
MARV/Pred.
700
710
720
730
ZEBOV SLEEEYPPWLTEKEAMNEENRFVTLDGQQFYWPVMNHKNKFMAILQHHQ
BDBV SLEDEYPPWLSEKEAMNEDNRFITMDGQQFYWPVMNHRNKFMAILQHHR
TAFV SLEGEHPPWLSEKEALNEDNRFITMDDQQFYWPVMNHRNKFMAILQHHK
MARV DLLQTNPPESLITALVEEYQNPVSAKELQADWPDMSFDERRHVAMNL
EBOV/X-ray
MARV/NMR
MARV/Pred.

Figure 7
Sequence alignment of NP$^{\rm Ct}$ from EBOV, TAFV, BDBV and MARV. Conserved residues are highlighted. Secondary-structure elements are as determined by crystallographic analysis for EBOV (Dziubańska *et al.*, 2014), TAFV and BDBV and by heteronuclear NMR for MARV (all from the present study). Helices are shown as tubes and β-strands as arrows. Also, an *in silico* prediction of two-dimensional elements for MARV as calculated by the consensus method using the GeneSilico Metaserver (Kurowski & Bujnicki, 2003) is shown at the bottom.

2014). The possibility that the MARV NP^{Ct} fragment is a molten globule with significant helical content (*e.g.* a three-helix bundle) prompted us to investigate the thermal stability of the protein using circular dichroism and to monitor the ellipticity at 222 nm (characteristic of α-helices). We observed the expected unfolding of the helical structure at $\sim$50°C (not shown), clearly indicating the presence of α-helices below this temperature.

4. Conclusions

Until recently, of the seven proteins encoded by the *Ebolavirus* genome, two have not yet had their structures characterized: the nucleoprotein (NP) and the RNA polymerase (L). Both of these proteins are critical for the assembly and replication of the virus and consequently are recognized as suitable drug targets. Our previous work on the C-terminal domain of the EBOV nucleoprotein (Dziubańska *et al.*, 2014), along with crystallographic analyses of the N-terminal, RNA-binding domain of the protein (Dong *et al.*, 2015; Leung *et al.*, 2015; Kirchdoerfer *et al.*, 2015), provides a foundation for future studies of the NP.

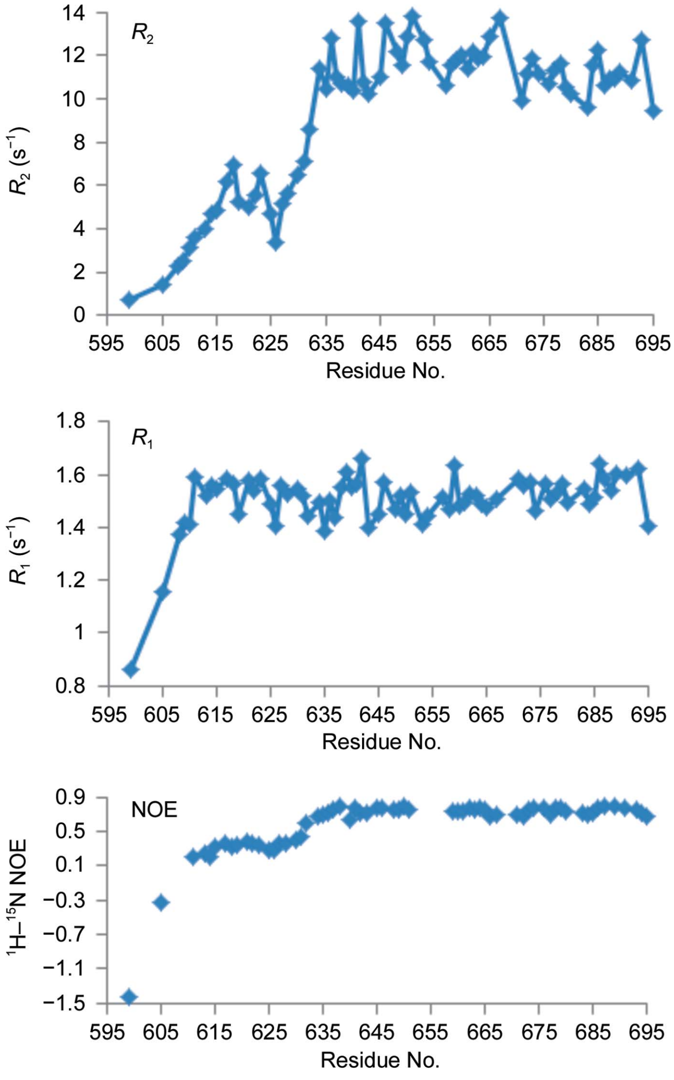

Figure 8

Spin–spin (R_2; top) and spin–lattice (R_1; middle) ^{15}N relaxation rates and ^{1}H–^{15}N nuclear Overhauser effects (NOE; bottom) *versus* residue number measured with a 600 MHz NMR spectrometer.

In this paper, we show that the homologous C-terminal domains of NP from two related pathogenic species of *Ebolavirus*, *i.e.* Taï Forest and Bundibugyo, have structures that are highly similar to that of the Zaire variant, in spite of differences in the amino-acid sequence. Interestingly, the related NP^{Ct} domain from MARV has a structure that was significantly different from the *Ebolavirus* consensus structure. This was not completely surprising: our alignment of the amino-acid sequences revealed that of the seven amino acids that constitute the hydrophobic core in this domain in the *Ebolavirus* NP^{Ct} only one (Trp722) is conserved. All others are significantly different: Phe688 to Thr, Leu692 to Glu, Pro697 to Ser, Phe731 to Arg, Ala733 to Val and Ile734 to Ala. The loss of a number of these hydrophobic residues is most likely to be responsible for the lack of a stable globular core and rationalizes why the MARV NP^{Ct} domain appears to be in a molten globule state.

Importantly, the *Ebolavirus* NP^{Ct} has also been identified as a possible target for the development of species-specific diagnostic tests (Sherwood & Hayhurst, 2013; Changula *et al.*, 2013; Niikura *et al.*, 2003). Structural characterization of NP^{Ct} from the different *Ebolavirus* species is relevant to this potential application.

Acknowledgements

The X-ray data-collection experiments were carried out at Argonne National Laboratory and specifically on beamlines operated by the Structural Biology Center (SCB) and South-Eastern Region Collaborative Access Team (SER-CAT) of the Advanced Photon Source. Argonne National Laboratory is operated by University of Chicago Argonne LLC for the US Department of Energy, Office of Biological and Environmental Research under Contract DE-AC02-06CH11357. Supporting institutions of SER-CAT may be found at http://www.ser-cat.org/members.html. Use of the Advanced Photon Source, an Office of Science User Facility operated for the US Department of Energy Office of Science by Argonne National Laboratory, was supported by US Department of Energy Contract DE-AC02-06CH11357. This research was supported by Research and Development and Ivy Foundation Biomedical Innovation grants from the University of Virginia (ZSD and DAE). We thank Ms Natalya Olekhnovich for technical assistance and Dr John H. Bushweller (UVA) for help with the NMR work.

References

Adams, P. D. *et al.* (2010). *Acta Cryst.* D**66**, 213–221.
Baize, S. *et al.* (2014). *N. Engl. J. Med.* **371**, 1418–1425.
Beniac, D. R., Melito, P. L., deVarennes, S. L., Hiebert, S. L., Rabb, M. J., Lamboo, L. L., Jones, S. M. & Booth, T. F. (2012). *PLoS One*, **7**, e29608.
Berjanskii, M. V. & Wishart, D. S. (2005). *J. Am. Chem. Soc.* **127**, 14970–14971.

Berman, H. M., Bhat, T. N., Bourne, P. E., Feng, Z., Gilliland, G., Weissig, H. & Westbrook, J. (2000). *Nature Struct. Biol.* **7**, 957–959.

Bharat, T. A., Noda, T., Riches, J. D., Kraehling, V., Kolesnikova, L., Becker, S., Kawaoka, Y. & Briggs, J. A. (2012). *Proc. Natl Acad. Sci. USA*, **109**, 4275–4280.

Brauburger, K., Hume, A. J., Mühlberger, E. & Olejnik, J. (2012). *Viruses*, **4**, 1878–1927.

Bukreyev, A. A. *et al.* (2014). *Arch. Virol.* **159**, 821–830.

Bunkóczi, G., Echols, N., McCoy, A. J., Oeffner, R. D., Adams, P. D. & Read, R. J. (2013). *Acta Cryst.* D**69**, 2276–2286.

Changula, K., Yoshida, R., Noyori, O., Marzi, A., Miyamoto, H., Ishijima, M., Yokoyama, A., Kajihara, M., Feldmann, H., Mweene, A. S. & Takada, A. (2013). *Virus Res.* **176**, 83–90.

Chen, V. B., Arendall, W. B., Headd, J. J., Keedy, D. A., Immormino, R. M., Kapral, G. J., Murray, L. W., Richardson, J. S. & Richardson, D. C. (2010). *Acta Cryst.* D**66**, 12–21.

Delaglio, F., Grzesiek, S., Vuister, G. W., Zhu, G., Pfeifer, J. & Bax, A. (1995). *J. Biomol. NMR*, **6**, 277–293.

Dong, S., Yang, P., Li, G., Liu, B., Wang, W., Liu, X., Xia, B., Yang, C., Lou, Z., Guo, Y. & Rao, Z. (2015). *Protein Cell*, **6**, 351–362.

Dziubańska, P. J., Derewenda, U., Ellena, J. F., Engel, D. A. & Derewenda, Z. S. (2014). *Acta Cryst.* D**70**, 2420–2429.

Emsley, P., Lohkamp, B., Scott, W. G. & Cowtan, K. (2010). *Acta Cryst.* D**66**, 486–501.

Ericsson, U. B., Hallberg, B. M., DeTitta, G. T., Dekker, N. & Nordlund, P. (2006). *Anal. Biochem.* **357**, 289–298.

Feldmann, H. & Geisbert, T. W. (2011). *Lancet*, **377**, 849–862.

Formenty, P., Boesch, C., Wyers, M., Steiner, C., Donati, F., Dind, F., Walker, F. & Le Guenno, B. (1999). *J. Infect. Dis.* **179**, S120–S126.

Heinig, M. & Frishman, D. (2004). *Nucleic Acids Res.* **32**, W500–W502.

Huang, Y., Xu, L., Sun, Y. & Nabel, G. J. (2002). *Mol. Cell*, **10**, 307–316.

Kirchdoerfer, R. N., Abelson, D. M., Li, S., Wood, M. R. & Saphire, E. O. (2015). *Cell. Rep.* **12**, 140–149.

Kneller, J. M., Lu, M. & Bracken, C. (2002). *J. Am. Chem. Soc.* **124**, 1852–1853.

Kolesnikova, L., Mühlberger, E., Ryabchikova, E. & Becker, S. (2000). *J. Virol.* **74**, 3899–3904.

Krissinel, E. & Henrick, K. (2007). *J. Mol. Biol.* **372**, 774–797.

Kurowski, M. A. & Bujnicki, J. M. (2003). *Nucleic Acids Res.* **31**, 3305–3307.

Leung, D. W. *et al.* (2015). *Cell. Rep.* **11**, 376–389.

Licata, J. M., Johnson, R. F., Han, Z. & Harty, R. N. (2004). *J. Virol.* **78**, 7344–7351.

Liu, Y., Stone, S. & Harty, R. N. (2011). *J. Infect. Dis.* **204**, S817–S824.

Mavrakis, M., Kolesnikova, L., Schoehn, G., Becker, S. & Ruigrok, R. W. (2002). *Virology*, **296**, 300–307.

Minor, W., Cymborowski, M., Otwinowski, Z. & Chruszcz, M. (2006). *Acta Cryst.* D**62**, 859–866.

Mühlberger, E., Weik, M., Volchkov, V. E., Klenk, H. D. & Becker, S. (1999). *J. Virol.* **73**, 2333–2342.

Murshudov, G. N., Skubák, P., Lebedev, A. A., Pannu, N. S., Steiner, R. A., Nicholls, R. A., Winn, M. D., Long, F. & Vagin, A. A. (2011). *Acta Cryst.* D**67**, 355–367.

Newman, J. (2005). *Acta Cryst.* D**61**, 490–493.

Niikura, M., Ikegami, T., Saijo, M., Kurata, T., Kurane, I. & Morikawa, S. (2003). *Clin. Diagn. Lab. Immunol.* **10**, 83–87.

Noda, T., Ebihara, H., Muramoto, Y., Fujii, K., Takada, A., Sagara, H., Kim, J. H., Kida, H., Feldmann, H. & Kawaoka, Y. (2006). *PLoS Pathog.* **2**, e99.

Noda, T., Watanabe, S., Sagara, H. & Kawaoka, Y. (2007). *J. Virol.* **81**, 3554–3562.

Painter, J. & Merritt, E. A. (2006). *Acta Cryst.* D**62**, 439–450.

Redfield, C. (2004). *Methods Mol. Biol.* **278**, 233–254.

Roddy, P., Howard, N., Van Kerkhove, M. D., Lutwama, J., Wamala, J., Yoti, Z., Colebunders, R., Palma, P. P., Sterk, E., Jeffs, B., Van Herp, M. & Borchert, M. (2012). *PLoS One*, **7**, e52986.

Sheffield, P., Garrard, S. & Derewenda, Z. (1999). *Protein Expr. Purif.* **15**, 34–39.

Shen, Y. & Bax, A. (2013). *J. Biomol. NMR*, **56**, 227–241.

Sherwood, L. J. & Hayhurst, A. (2013). *PLoS One*, **8**, e61232.

Shi, W., Huang, Y., Sutton-Smith, M., Tissot, B., Panico, M., Morris, H. R., Dell, A., Haslam, S. M., Boyington, J., Graham, B. S., Yang, Z.-Y. & Nabel, G. J. (2008). *J. Virol.* **82**, 6190–6199.

Vagin, A. & Teplyakov, A. (2010). *Acta Cryst.* D**66**, 22–25.

Vranken, W. F., Boucher, W., Stevens, T. J., Fogh, R. H., Pajon, A., Llinas, P., Ulrich, E. L., Markley, J. L., Ionides, J. & Laue, E. D. (2005). *Proteins*, **59**, 687–696.

Walczak, M. J., Samatanga, B., van Drogen, F., Peter, M., Jelesarov, I. & Wider, G. (2014). *Angew. Chem. Int. Ed.* **53**, 1320–1323.

Watanabe, S., Noda, T. & Kawaoka, Y. (2006). *J. Virol.* **80**, 3743–3751.

Winn, M. D. *et al.* (2011). *Acta Cryst.* D**67**, 235–242.

Wukovitz, S. W. & Yeates, T. O. (1995). *Nature Struct. Mol. Biol.* **2**, 1062–1067.